CAMBRIDGE
UNIVERSITY PRESS

Article

Crystal chemistry of zemannite-type structures: IV. Wortupaite, the first new tellurium oxysalt mineral described from an Australian locality

Owen P. Missen[1,2,3] (ID), Stuart J. Mills[1] (ID), Joël Brugger[2] (ID), William D. Birch[1] (ID) and Peter Elliott[4,5] (ID)

[1]Geosciences, Museums Victoria, GPO Box 666, Melbourne 3001, Victoria, Australia; [2]School of Earth, Atmosphere and Environment, Monash University, Clayton 3800, Victoria, Australia; [3]Centre for Ore Deposit and Earth Sciences (CODES), University of Tasmania, Hobart, Australia; [4]School of Physical Sciences, The University of Adelaide, Adelaide, South Australia 5005, Australia; and [5]South Australian Museum, North Terrace, Adelaide, South Australia 5000, Australia

Abstract

Wortupaite (IMA2022–107) is a new hydrated magnesium nickel tellurite mineral with a zemannite-like structure, described from the Wortupa gold mine, South Australia, Australia. Wortupaite forms needles up to 25 μm in length, generally clustered and sometimes in blocky masses of shorter (10−15 μm) crystals. Wortupaite is found growing on melonite, from which the component nickel and tellurium are derived, and is associated with calcite. The strongest powder diffraction lines are [d_{obs}Å(I_{obs})(hkl)]: 8.059 (93) (100), 4.034 (92) (200), 2.832 (43) (211 and 121), 2.769 (100) (202) and 1.920 (45) (213 and 123). The empirical formula of wortupaite as determined by electron probe microanalysis is $(Mg_{0.57}Ni_{0.39}Mn_{0.04})_{\Sigma1}(Ni^{2+}_{1.87}Fe^{3+}_{0.13})_{\Sigma2}(Te^{4+}O_3)_3 \cdot 3H_2O$, simplified to the ideal formula of $MgNi^{2+}_2(Te^{4+}O_3)_3 \cdot 3H_2O$ with H_2O content calculated from the crystal structure. The average crystal structure of wortupaite was determined by single-crystal X-ray diffraction with synchrotron radiation ($R_1 = 0.0558$ for 100 independent reflections). Wortupaite is hexagonal, crystallising in the space group $P6_3/m$, with $a = 9.2215(13)$ Å, $c = 7.5150(15)$ Å, $V = 553.43(19)$ Å^3 and $Z = 2$. Wortupaite has a microporous structure, with the negatively charged zemannite-like framework formed by $Te^{4+}O_3$ trigonal pyramids and $Ni^{2+}O_6$ octahedra. For charge balance, Mg^{2+} and Ni^{2+} dominant sites are assumed to be located on central sites in the channels, coordinated by 6 H_2O groups. An OW site was refined around the Mg^{2+} dominant site, but OW position(s) were not locatable around the Ni^{2+} dominant site. A discussion of the different models for crystallographic arrangement of channel species is provided, taking into account possible Fourier truncation effects. Unlike the other four minerals with zemannite-like structures which have a near 50% split of divalent and trivalent framework cations, wortupaite is the first natural phase to have only divalent cations in the framework sites.

Introduction

Tellurium (Te) is a very rare element (crustal abundance 1 ppb) that forms ~200 described minerals, making it the most anomalously diverse element when comparing crustal abundance to number of minerals (Christy, 2015). This high number of described minerals may be explained by the wide range of geochemical niches which Te fills (Brugger *et al*, 2012; Grundler *et al.*, 2013; Krivovichev *et al.*, 2020). While both a chemically and structurally diverse group of minerals, the majority (70 out of 100, 70%) of tellurium oxysalts have been described from a small geographical area of south-western North America. For instance, Moctezuma, Sonora, Mexico (21 new minerals) and Otto Mountain, California, USA (16 new minerals) have

contributed 37 of the 100 known Te–O minerals between them. All other countries have contributed just 29 new Te–O minerals, of which Australia had previously contributed none. The only new Te minerals previously described in Australia were three rare tellurides found in Western Australia; namely honeaite (Au_3TlTe_2; Rice *et al.*, 2016; Welch *et al.*, 2017), kalgoorlieite (As_2Te_3; Rempel and Stanley, 2016) and saddlebackite ($Pb_2Bi_2Te_2S_3$; Clarke, 1997). Wortupaite thus represents the first tellurium oxysalt mineral to be described from Australia, and just the sixth new mineral in the Southern Hemisphere after brumadoite from Pedra Preta Pit, Bahia, Brazil (Atencio *et al.*, 2008) and four minerals from the Tambo mine, Coquimbo, Chile: walfordite (Back *et al.*, 1999), telluromandarinoite (Back *et al.*, 2017), and tamboite and metatamboite (Cooper *et al.*, 2019).

Wortupaite has a unique chemical composition amongst natural compounds, being the first mineral to contain only Mg, Ni and Te as the metallic cations. Keystoneite is the only other Ni-containing secondary Te mineral described to date, though keystoneite also contains Fe^{3+} (Missen *et al.*, 2021). Wortupaite

shares an isotypic framework with zemannite (Miletich, 1995a; Cametti *et al.*, 2017, Missen *et al.*, 2019a; Effenberger *et al.*, 2023), kinichilite (Koyama and Nagashima, 1981; Miletich, 1995a), keystoneite (Missen *et al.*, 2021) and ilirneyite (Pekov *et al.*, 2018). All four of these minerals have a near 50% split of divalent (Zn^{2+}, Mn^{2+} or Ni^{2+}) and trivalent (Fe^{3+} and Mn^{3+}) cations, making wortupaite the first natural zemannite-structured phase to have only divalent cations in the framework sites.

The name and formula (symbol Wor) of wortupaite (IMA2022−107) have been approved by the Commission on New Minerals Nomenclature and Classification (CNMNC) of the International Mineralogical Association (IMA) (Missen *et al.*, 2023). Wortupaite is named for the type locality. The name 'Wortupa' means 'shadow' in the language of the local indigenous people, the Adnyamathanha. Type material is deposited in the collections of Museums Victoria, Melbourne, Australia with specimen number M2021.

Occurrence and paragenesis

Wortupaite occurs at the Wortupa gold mine (Fig. 1), 12 km north-north-east of Balcanoona Station, Flinders Ranges, South Australia, Australia (30.437966°S, 139.24237°E). Gold was discovered in 1899, however shallow workings provided poor returns and work ceased by 1905. The National Museum of Victoria (as Museums Victoria was then known) purchased the holotype sample on the 12th of September, 1900 from James Mitchell. The mineralisation consists of irregular veins, lenses and pods of quartz and calcite, with scattered crystals of pyrite and disseminated malachite within scapolitised limestone (Hamisi *et al.*, 2023) and calcareous siltstones of the Neoproterozoic Adelaide geosyncline (Coats and Blissett, 1971). Wortupaite is the first new mineral described from this locality.

Associated minerals

Wortupaite is intimately associated with nickel telluride mineral melonite ($NiTe_2$), upon which it is found growing. Calcite is the gangue mineral on the holotype specimen. Other minerals previously identified from the Wortupa mine include quartz, native gold, pyrite, chalcocite, malachite, azurite and goethite, as well as scapolite (Coats and Blissett, 1971), however none of these were observed on the holotype specimen.

Origin of the mineral

The first evidence of Te secondary minerals at the Wortupa mine was reported by Higgin (1899) when he noted a green coating associated with melonite and suspected that it was "probably a tellurite of nickel". Wortupaite formed after oxidation of melonite, from which its major component elements (Ni and Te) were derived, probably under near-surface conditions. The Mg^{2+} in wortupaite was most likely to have been leached from minerals such as magnesite or Mg-silicates in associated sedimentary rocks, which then mixed with the Ni- and Te-rich fluids produced on the surface of weathering melonite to form wortupaite.

Appearance, physical, and optical properties

Wortupaite forms pale yellowish green needles and prisms, often in clusters and blocky masses (Fig. 2). The needles may reach 25 µm in length, but are generally shorter with a lower length


Figure 1. The small workings of the eponymous Wortupa mine, where few primary sulfides (aside from scattered pyrite) and no telluride mineralised zones remain. (a) Author JB surveys a former tailings pile. (b) Mine entrance surrounded by non-mineralised pebbles. Photos taken in November 2017.

to diameter ratio. Wortupaite has prismatic $\{10\bar{1}0\}$ forms, with prisms terminated by $\{10\bar{1}1\}$ (Fig. 3). The *c:a* ratio is 0.8149 (single-crystal X-ray diffraction data) and no evidence for
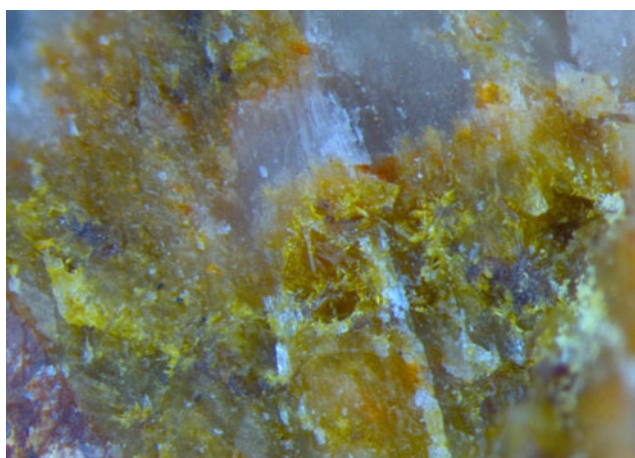
Figure 2. Optical image of holotype wortupaite specimen (Museums Victoria M2021), showing yellowish green wortupaite crystals on calcite.
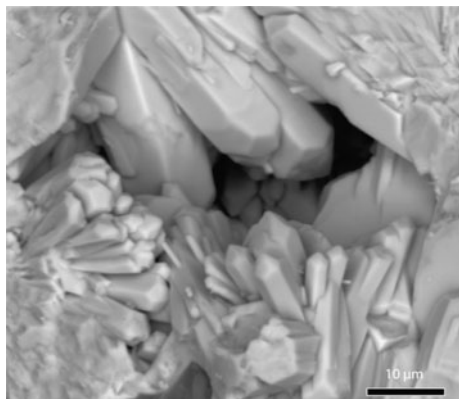
Figure 3. Scanning electron microscopy images of holotype wortupaite specimen (Museums Victoria M2021) showing bunches of hexagonal prismatic needles analogous to zemannite.

twinning was observed. Wortupaite has a pale-green streak, and individual crystals are vitreous, whereas masses have a more earthy lustre. Wortupaite does not fluoresce. Mohs hardness was not determinable but is likely to be < 3, analogous to zemannite. The fracture is uneven, tenacity is brittle and neither cleavage nor parting was observed. The density was calculated to be 4.42 g/cm^3 for the empirical formula and unit cell volume refined from single-crystal X-ray diffraction data. The indices of refraction of wortupaite are higher than the liquids available for their measurement. The average refractive index (n_{ave}) was calculated from the Gladstone–Dale compatibility index as 1.907, using the unit cell used for the crystal-structure refinement. ω and ε were calculated from n_{ave} after measuring the ω–ε birefringence [0.075(10), using a Bertrand lens and a 530 nm gypsum plate]. Wortupaite is uniaxial (+), with ω(calc) = 1.882(10) and ε(calc) = 1.957(10). Neither dispersion nor orientation was observed. Faint pleochroism was observed, with *O* = green–blue, *E* = yellow with green tinge and *O* > *E*.

X-ray photoelectron spectroscopy

X-ray photoelectron spectroscopy (XPS) was conducted using a Nexsa Surface Analysis System at the Monash X-ray Platform (MXP) of Monash University, Clayton, Australia, and data were processed using *Avantage* software (both by Thermo Fisher Scientific). X-rays were generated with a Mg target producing *K*α radiation with a beam diameter of 100 μm. The binding energy scale was referenced to amorphous C1*s* at 284.5 eV. A full-range spectrum was collected prior to collecting detailed scans in the Ni2*p* (845–885 eV) and Te3*d* regions (560–600 eV).

The XPS spectrum in the Te3*d* region shows two peaks at 575.3 and 585.9 eV corresponding to the $3d_{5/2}$ and $3d_{3/2}$ peaks of Te^{4+}, based on comparison with the reference compound TeO$_2$ that displays Te^{4+} peaks at 576.3 and 586.7 eV (Thermo Fisher, 2013–2021).

The XPS spectrum in the Ni2*p* region shows a peak at 855.2 eV and a satellite at 861.4 eV, then a peak at 872.6 eV and a satellite at 878.7 eV which correspond to the $2p_{3/2}$ and $2p_{1/2}$ peaks of Ni^{2+}, respectively, based on comparison with the reference compound NiO that shows a combined peak at 855.1 eV, satellite at 860.5 eV and then a second peak at 872.4 eV with satellite at 879.5 eV (Thermo Fisher, 2013–2021). No evidence of any Ni^{3+} was observed in the XPS spectra.

Chemical composition

Chemical analytical data were collected using electron probe microanalysis (EPMA) on a JEOL JXA-8530F Field Emission Electron Microprobe (wavelength dispersive spectroscopy mode, 15 kV, 5 nA, 20 μm beam diameter), at the School of Earth Sciences, University of Melbourne, Australia (see Table 1). All other elements were below detection limits, including Zn. The ratio of atoms per formula unit (apfu) calculated on the basis of 9 O apfu for the anhydrous part is $Mg_{0.57}Mn_{0.04}Ni_{2.26}Fe_{0.13}$ $Te_{3.00}O_9 \cdot 3H_2O$ and the empirical formula is $(Mg_{0.57}Ni_{0.39}$ $Mn_{0.04})_{\Sigma1.00}(Ni_{1.87}^{2+}Fe_{0.13}^{3+})_{\Sigma2.00}(Te^{4+}O_3)_3 \cdot 3H_2O$. The ideal formula is $MgNi_2^{2+}(Te^{4+}O_3)_3 \cdot 3H_2O$, which requires MgO 5.58, NiO 20.68, TeO$_2$ 66.27, H$_2$O 7.48, total 100 wt.%. H$_2$O content was calculated from the crystal structure as 3 H$_2$O groups pfu, although up to 6 H$_2$O pfu is the maximum possible hydration (see Crystal structure discussion below). It is worth noting that with 3 H$_2$O groups pfu, the total of the EPMA data is 99.99 wt.%.

X-ray crystallography and structure refinement

Powder X-ray diffraction

Powder X-ray diffraction (XRD) data were collected using an Oxford Xcalibur 2 system with Sapphire2 CCD and MoKα radiation (50 kV and 1 mA) at 293(1) K. A Gandolfi-type randomised crystal movement was achieved by rotations on the φ and ω axes. Data are presented in Table 2. The unit-cell parameters refined from the powder XRD pattern with whole pattern fitting using *ChekCell* software (Laugier and Bochu, 2004) are *a* = 9.327(9) Å and *c* = 7.5946(3) Å.

Single-crystal X-ray diffraction

Single-crystal XRD data were collected on the micro-focus macromolecular MX2 beamline at the Australian Synchrotron, part of ANSTO. A 5 × 5 × 15 μm prism of wortupaite was selected from specimen M2021 by crushing an aggregate of crystals in oil then selecting a single-crystal fragment. We tested a number of crystal fragments from the type specimen, with the chosen crystal being the best diffractor despite providing only an average of 5 distinct spots per frame. Data were collected at 100 K by a Dectris EigerX 16M detector using monochromatic radiation with a wavelength of 0.71073 Å, collecting a full 360° of data with 1° step size and 1 second per step. The data were processed using *XDS* (Kabsch, 2010), *XPREP* (Bruker, 2001) and *SADABS* (Bruker, 2001), finding 1830 reflections with R_{int} of 0.1031. Despite this low number of reflections, the crystal structure of the framework of wortupaite was readily refined, and a model for the arrangement of the channel species is presented below.

Table 1. Composition of wortupaite (in wt.%) from EPMA.

Constituent	Mean	Range	S.D.	Reference
MgO	3.13	2.52–3.50	0.3	Forsterite
MnO	0.38	0.30–0.47	0.06	Mn metal
Fe$_2$O$_3$	1.53	0.96–2.44	0.5	Fe$_2$O$_3$
NiO	22.83	21.88–23.70	0.6	NiFe
TeO$_2$	64.76	64.27–65.18	0.3	TeO$_2$ (syn)
H$_2$O*	7.36			
Total	99.99			

*H$_2$O calculated from crystal structure.

S.D. = standard deviation (σ)

Table 2. Powder XRD data (*d* in Å) for wortupaite with comparisons to zemannite and keystoneite shown for comparison.*

Type wortupaite (Museums Victoria M2021) This study			Crystal structure This study			Type keystoneite (Canadian Museum of Nature CMN56561) (Missen *et al.*, 2021)		Calculated pattern for type zemannite (ROM M25933) (Missen *et al.*, 2019a)	
I_{obs}	d_{obs}	hkl	I_{calc}	d_{calc}		I_{obs}	d_{obs}	I_{obs}	d_{obs}
93	**8.059**	**1 0 0**	**100**	**7.986**		90	8.12	100	8.130
92	**4.034**	**2 0 0**	**72**	**3.993**		80	4.05	48	4.065
19	3.789	0 0 2	14	3.757		40	3.81	10	3.814
4	3.438	1 0 2	3	3.400		20	3.443	4	3.453
15	3.054	2 1 0, 1 2 0	6, 5	3.018, 3.018		30	3.063	7, 6	3.073,3.073
18	2.950	1 1 2	13	2.913		50	2.952	18	2.960
43	**2.832**	**2 1 1, 1 2 1**	**10, 19**	**2.801, 2.801**		50	2.838	**19, 6**	**2.850, 2.850**
100	**2.769**	**2 0 2**	**79**	**2.736**		100	2.774	57	2.781
14	2.537	3 0 1	9	2.509		30	2.543	8	2.554
		2 1 2, 1 2 2	1, 4	2.353, 2.353		20	2.381	5, 1	2.393, 2.393
30	2.332	2 2 0	17	2.305		35	2.337	13	2.347
9	2.197	3 0 2	6	2.172		20	2.200	8	2.209
10	2.147	3 1 1, 1 3 1	3, 1	2.125, 2.125		30	2.151	2, 5	2.162, 2.162
15	1.987	2 2 2	8	1.965		40	1.991	5	1.999
45	**1.920**	**2 1 3, 1 2 3**	**2, 0**	**1.928, 1.928**		30	1.951	**0, 2**	**1.959, 1.959**
13, 8	1.896, 1.850	0 0 4	3	1.879		35	1.849	2, 2	1.856, 1.854
12	1.798	2 3 1, 3 2 1	2,4	1.780, 1.780		30	1.802	4, 1	1.812, 1.812
22	1.782	4 0 2	10	1.763		30	1.784	9	1.794
39	1.718	2 0 4	11	1.700		60	1.720	9	1.726
9	1.678	3 1 3, 1 3 3	5,0	1.659, 1.659		30	1.682	0, 7	1.687, 1.687
9	1.581	5 0 1	5	1.562		20	1.584	4	1.590
18	1.495	3 2 3, 2 3 3	6,4	1.478, 1.478		45	1.498	8, 3	1.504, 1.504

*The five strongest observed lines are highlighted in bold. Cutoff: averaged *I* >5.

Structure solution of the average structure of wortupaite was carried out by direct methods using *SHELXT* (Sheldrick, 2015a) followed by structure refinement in *SHELXL* (Sheldrick, 2015b). All atom positions and anisotropic displacement parameters for Ni and Te only were refined to final R_1 and wR_2 values (all data) of 0.0558 and 0.1393, respectively. Further details of data collection and structure refinement are provided in Table 3. Atomic coordinates and displacement parameters are shown in Table 4, selected bond-lengths in Table 5 and a bond-valence analysis in Table 6, using parameters of Gagné and Hawthorne (2015) for all atoms except Te (Mills and Christy, 2013). The crystallographic information files have been deposited with the Principal Editor of *Mineralogical Magazine* and are available as Supplementary material (see below).

Space group for wortupaite

The space-group in which zemannite-like minerals and compounds crystallise in has generally focused on two hexagonal space-groups: centrosymmetric $P6_3/m$ and non-centrosymmetric $P6_3$. Recent work has proposed a trigonal $P3$ symmetry for zemannite due to a different ordering scheme of the M^{2+} and M^{3+} cations within the framework of the zeolitic structure (Effenberger *et al.*, 2023). The influence of framework cation ordering and also the H-bonding network leads to a non-centrosymmetric refinement in zemannite (Cametti *et al.*, 2017, Missen *et al.*, 2019a). However, synthetic zemannite-like compounds $Na_2[Co_2(TeO_3)_3] \cdot 3H_2O$ and $Na_2[Zn_2(TeO_3)_3] \cdot 3H_2O$ (Miletich, 1995b), which have only one framework transition metal cation crystallise in centrosymmetric $P6_3/m$. Refinements in both space groups were explored for wortupaite, with the centrosymmetric refinement preferred for the final refinement as the non-centrosymmetric setting did not give a stable structural

refinement. The issue with the non-centrosymmetric refinement included a Flack parameter close to ½, and the presence of non-positive definite atoms such as the channel Mg^{2+} and framework

Table 3. Crystal structure refinement details for wortupaite.

Crystal data

Ideal chemical formula	$MgNi_2^{2+}(Te^{4+}O_3)_3 \cdot 3H_2O$ (H positions not located)
Crystal system, space group	Hexagonal, $P6_3/m$
Temperature (K)	100(1)
a, c (Å)	9.2215(13), 7.5150(15) Å
V (Å³)	553.43(19)
Z	2
Calculated density (g cm⁻³)	4.385
Radiation type and wavelength (Å)	Synchrotron, λ = 0.71073
μ (mm⁻¹)	11.877
Crystal dimensions (mm)	0.005×0.005×0.015
Reflections for cell refinement	899, 2.27–20.00°2θ

Data collection

Crystal description	Pale yellowish green prism
Diffractometer	Dectris EigerX 16M
θ (°) range	2.550–25.542
Indices range of *h, k, l*	*h*: ±7, *k*: ±7, *l*: ±5
Absorption correction	Multi-scan *SADABS*
T_{min}, T_{max}	0.2393, 0.4226
No. of measured, independent and observed $[I > 2\sigma(I)]$ reflections	1830, 100, 94
R_{int}	0.1031
Data completeness to 25.542°θ (%)	100

Refinement

Number of reflections, parameters, restraints	100, 21, 0
$R_1[F^2 > 2\sigma(F^2)]$, R_1(all)	0.0544, 0.0558
$wR_2[F^2 > 2\sigma(F^2)]$, wR_2(all)	0.1378, 0.1393
GoF (F^2)	1.168
$\Delta\rho_{min}$, $\Delta\rho_{max}$ ($e^- $ Å⁻³)	−0.79, 1.81

Table 4. The atom coordinates and displacement parameters from the crystal structure refinement for wortupaite.

Atom	x/a	y/b	z/c	Occ	U_{eq} / U_{iso}	
Te1	0.5371(5)	0.4968(4)	¾	1	0.033(3)	
M1	⅔	⅓	0.4304(11)	$Ni_{0.93}Fe_{0.07}$	0.026(3)	
O1	0.340(4)	0.497(3)	¾	1	0.011(9)	
O2	0.482(3)	0.341(3)	0.566(3)	1	0.033(7)	
M2	0	0	¾	$Mg_{0.42}Ni_{0.08}$	Fixed 0.05	
M3	0	0	0.846(6)	$Mg_{0.075}Ni_{0.155}Mn_{0.02}$	Fixed 0.05	
OW	0.146(6)	0.199(6)	0.930(7)	0.50	Fixed 0.05	
	U^{11}	U^{22}	U^{33}	U^{23}	U^{13}	U^{12}
Te1	0.036(4)	$= U^{11}$	0.027(4)	0	0	$= U^{11}/2$
M1	0.032(4)	$= U^{11}$	0.014(6)	0	0	$= U^{11}/2$

O sites). Additionally, lower symmetry space groups are also possible for zemannite, with recent examples of lower symmetry found in monoclinic twin domains in zemannite-structured $K[(Cu^{2+},Mn^{2+},Mn^{3+})_2(TeO_3)_3]\cdot 2H_2O$ (Eder *et al.*, 2023b). Refinements in $P2_1/m$ and $P\bar{6}$ were also undertaken but did not result in improved statistics for wortupaite.

Crystal structure description: framework

The crystal structure of wortupaite (Fig. 4) is similar to that of zemannite, with a characteristic host-guest structure (Cametti *et al.*, 2017; Missen *et al.*, 2019a; Effenberger *et al.*, 2023). Like zemannite, wortupaite is a zeolitic tellurite mineral containing isolated *neso* $Te^{4+}O_3^{2-}$ pyramids (Christy *et al.*, 2016), linked into a three-dimensional microporous framework by face-sharing Ni_2O_9 octahedra. The $Te^{4+}O_3^{2-}$ pyramids feature a typically bimodal bond-length distribution, with three short strong bonds forming the trigonal pyramid with an average Te–O distance of 1.85 Å, and four (2×2) long, weak secondary Te–O bonds with an average length of 3.03 Å (Christy and Mills, 2013) resulting in a total bond-valence sum of 4.26 valence units (vu). Nickel (with minor substitution by Fe^{3+}, represented in the crystal structure as $M1$) is coordinated by six O anions with a bimodal distribution: three shorter Ni1–O2 bonds with length 2.02(2) Å and three longer Ni1–O1 bonds with length 2.10(2) Å.

The structures of zemannite and wortupaite differ with regards to the valence of the framework cations, geometry of $M(H_2O)_6$ clusters in the channels and also by the presence of two (rather than one) extra-framework cation site within the channels for charge balance. In zemannite (and all other zemannite-framework minerals described to date, see below), half of the framework cations are divalent and the other half are trivalent, leading to an ordered arrangement (Missen *et al.*, 2019a; Effenberger *et al.*, 2023). In wortupaite, all the framework cations are divalent and Ni-dominant, with no ordering by definition. The wortupaite framework has a higher negative charge (−2 in ideal wortupaite) than zemannite (−1), leading to a different arrangement of channel

species than the half-occupied octahedral $Mg(H_2O)_6$ complexes typical of zemannite, kinichilite, ilirneyite and keystoneite.

Crystal structure description: channels

Due to the low levels of diffraction from wortupaite crystals and correspondingly low number of reflections collected in the refinement, the refinement of channel species is not unambiguous. The data are subject to Fourier truncation effects which means that the highest peaks in the difference-Fourier map (i.e. those in the channel) may originate from not having sufficient Fourier coefficients. In this section, we present the best model we refined: the model with EPMA fitted across three metal sites (one framework site, two channel sites). The crystallographic information file of the unrefined model ($M1$ as Ni, $M2$ as Mg and $M3$ as Ni) is also provided in Supplementary material. Once the framework species are refined, the largest remaining peak in the difference-Fourier map is at (0 0 ¾) and with a site-scattering value of ~8.6 e^-, indicating less than full occupation by the $M2^{2+}$ cation, modelled initially as a partially occupied Mg^{2+} site (again noting that the high value of z i.e. ¾ is potentially due to Fourier truncation effects). The largest peak following the refining of the first peak is at (0 0 0.86), with site scattering of ~5 e^-, modelled initially as a partially occupied Ni^{2+} site ($M3^{2+}$ cation). Both of these sites were refined with fixed U_{iso} values of 0.05. Refinement allowing the site occupancies to vary results in an initial tunnel composition of $M2_{0.60}M3_{0.43}$, close to the ideal cation requirement of 1.0 cations pfu. Thus, the required M^{2+} content of the channels, $(Mg_{0.57}Ni_{0.39}Mn_{0.04})_{\Sigma 1.00}$ pfu, as indicated by the EPMA data, can be reasonably attributed to two sites, i.e. $M2(2a)$ $(Mg_{0.42}Ni_{0.08})_{\Sigma 0.5}$ pfu at (0 0 ¾) and $M3$ $(4e)$ $(Mg_{0.15}Ni_{0.31}Mn_{0.04})_{\Sigma 0.5}$ pfu at (0 0 0.846(6)) based on the site-scattering factors. Fitting occupancies with the EPMA data changes the R indices by less than 0.05%.

Table 6. Bond-valence table for wortupaite.

Atom	Te1	M1	M2	Σ
O1	1.44	0.31 (×3↓, ×2→)		2.07
O2	1.25, 0.11, 0.05 (All ×2↓)	0.39 (×3↓)		1.80
OW			0.29 (×6↓)	0.29
Σ	4.26	2.11	1.74	

Bond-valence parameters for all elements taken from Gagné and Hawthorne (2015) except for Te (Mills and Christy, 2013). $M1$: $Ni_{0.93}Fe_{0.07}$ and $M2$: $Mg_{0.42}Ni_{0.08}$. Bond valence for the $M3$ site is not calculable as it is probably coordinated by a different OW site(s), not detectable in this crystal structure refinement Fourier map.

Table 5. Selected bond lengths for wortupaite.

Te1–O1	1.81(3)	$M1$–O2 ×3	2.02(2)	
Te1–O2 ×2	1.87(2)	$M1$–O1 ×3	2.10(2)	
Te1–O2 ×2	2.86(2)	<$M1$–O>	2.06	
Te1–O2 ×2	3.19(2)			
<Te1–O$_{short}$>	1.85	$M2$–OW ×6	2.13(5)	
<Te1–O$_{long}$>	3.03			

$M1$: $Ni_{0.93}Fe_{0.07}$ and $M2$: $Mg_{0.42}Ni_{0.08}$. Bond-lengths for the $M3$ site are not shown as it is probably coordinated by a different OW site(s), not detectable in this crystal structure refinement Fourier map.
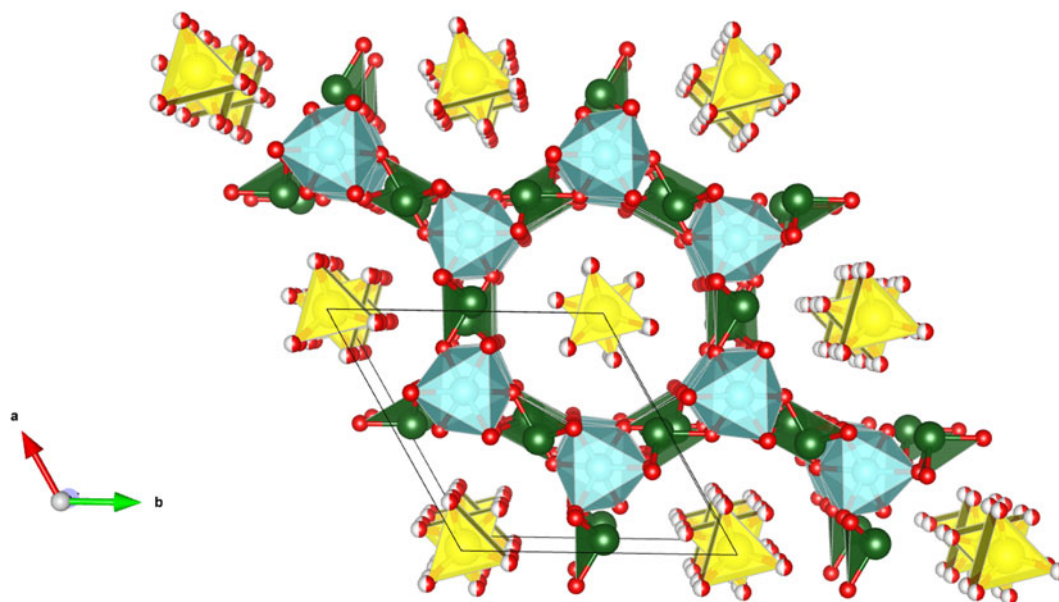
Figure 4. The structure of wortupaite viewed down *c*. Te^{4+}O$_3$ trigonal pyramids in dark green, Ni^{2+}O$_6$ octahedra in light blue and MgO$_6$ trigonal prisms (*M*2 shown only) in yellow. Drawn with Vesta (Momma and Izumi, 2011).

The highest remaining difference-Fourier peak (site-scattering factor ~2 e^-) is at an appropriate distance from the channel cation sites and from framework O1 and O2 sites to be an OW site, defined as 50% occupied to avoid unreasonably short OW–OW distances and again positionally refined using a fixed U_{iso} value of 0.05. The clear preference for the OW sites in wortupaite is for an arrangement around *M*2 showing significant distortion away from octahedral coordination (Fig. 5). The addition of the half-occupied OW site to the model lowers the R_1(all) to 0.054 from 0.076. Given the limited nature of the dataset, it is possible that this site is related to disorder or Fourier truncation effects, but we have chosen to present the final model including the O sites for completeness of the *M*2 coordination sphere (*M*2–OW: 2.13(5) Å × 6) (Fig. 5). It is worth noting that the quarter-occupied *M*3 (Ni-dominant) channel site is not expected to be coordinated by the half-occupied OW site in its refined position (which with *M*3 would display a one-sided coordination featuring three *M*3–OW bonds at 1.77(5) Å and three at 2.36(6) Å). Both the one-sided coordination and bonds to OW with distance <1.80 Å are essentially impossible for O ligand geometry around the *M*3 transition metal-dominant cation. Instead, *M*3 may be expected to be coordinated by two additional 12*i* sites ('OW2' and 'OW3') for 6-fold coordination, but such low-scattering sites were not locatable in the Fourier map of the available refinement data. This possibility also suggests that wortupaite may have a hydration > 3H$_2$O groups per formula unit (up to 6H$_2$O groups pfu possible as a maximum). We also explored the possibility for the OW sites (isotropic displacement parameter of the single position, if refined, is > 0.05 Å^2) to be disordered over multiple sites − which would allow for a more symmetric stereochemical arrangement of OW sites around *M*3, as well as a reasonable geometry and bond-valence sum, however this attempted refinement was unstable. In the synthetic zemannite-like compound of Eder *et al.* (2023a) with the formula K$_2$[Co$_2$(TeO$_3$)$_3$]·2.5H$_2$O, channel cation positions were found in positions similar to those of the OW sites in wortupaite. We tried to refine a model with the channel cation sites away from the centre of the channel, but the refinement was also unstable.

Relationship to other species

Wortupaite is structurally most closely related to the two synthetic zemannite-like compounds, Na$_2$[Co$_2$(TeO$_3$)$_3$]·3H$_2$O and Na$_2$[Zn$_2$(TeO$_3$)$_3$]·3H$_2$O (Miletich, 1995b), which also have frameworks with a formal −2 charge. Other related compounds include a selenite analogue of the zemannite structure type, K$_2$[Ni$_2$(SeO$_3$)$_3$]·2H$_2$O (Wildner, 1993), and an unpublished Sr-dominant Co zemannite, Sr$_x$[Co$_2$(SeO$_3$)$_3$]·yH$_2$O (Wildner, 1993), the latter featuring a fully occupied divalent channel cation (Sr^{2+}). Ni–O bond lengths in the Ni^{2+}O$_6$ octahedra of
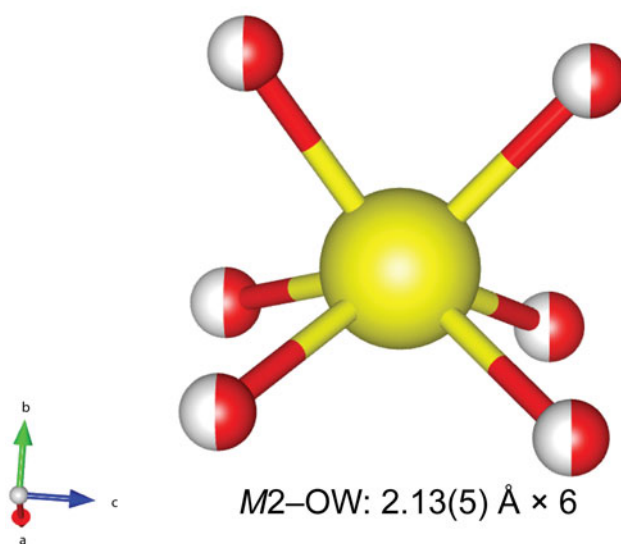
Figure 5. *M*2 geometry in wortupaite, with the Mg-dominant site showing symmetrical MgO$_6$ trigonal prisms.

$K_2[Ni_2(SeO_3)_3]\cdot 2H_2O$ are two triplets of 2.057(3) Å and 2.137(4)Å (average 2.097 Å). The Na^+-containing compounds such as $Na_2[Co_2(TeO_3)_3]\cdot 3H_2O$ usually have Na^+ cations situated near the edges of the microporous channels, rather than in the centre as is typical for zemannite. A series of mainly cryptocrystalline zemannite-like compounds with Na^+ in the centre of the microporous channels (compositions ranging from $Na_{1.25}Fe^{3+}_{0.75}Zn_{1.25}(TeO_3)_3\cdot 3H_2O$ to $Na_{0.55}Fe^{3+}_{1.44}Zn_{0.56}(TeO_3)_3\cdot 3H_2O$) have also been synthesised (Missen *et al.*, 2019b). In the studied sample of wortupaite, two partially-occupied channel cation sites were located [at different positions with coordinates in the form (0 0 *z*)]. The only previously described naturally occurring Ni-bearing Te oxysalt keystoneite, ideally $Mg_{0.5}Ni^{2+}Fe^{3+}(TeO_3)_3\cdot 4H_2O$, has Ni–O bonds with an average length of 2.085 Å. In addition, several new zemannite-like compounds have recently been reported for the first time, including Ni-bearing $Na_2[Ni_2(TeO_3)_3]\cdot 2.5H_2O$ and $K_2[Ni_2(TeO_3)_3]\cdot H_2O$ (Eder *et al.*, 2023a) and the first Jahn-Teller distorted framework in a zemannite-like structure observed in $K[(Cu^{2+},Mn^{2+},Mn^{3+})_2(TeO_3)_3]\cdot 2H_2O$ (Eder *et al.*, 2023b). The Ni-bearing compounds have Ni–O distances of 2.064 and 2.069 Å, respectively − close to the average 2.06 Å bond length in the wortupaite framework. There are likely to be many more zemannite-structured compounds yet to be discovered as minerals or to be synthesised in the laboratory.

References

Atencio D., Roberts A.C., Matioli P.A. Stirling J.A.R., Venance K.E. Doherty W., Stanley C.J., Rowe R. Carpenter G.J.C. and Coutinho J.M.V. (2008) Brumadoite, a new copper tellurate hydrate, from Brumado, Bahia, Brazil. *Mineralogical Magazine*, **72**, 1201−1205.

Back M.E., Grice J.D., Gault R.A., Criddle A.J. and Mandarino J.A. (1999) Walfordite, a new tellurite species from the Wendy open pit, El Indio-Tambo mining property, Chile. *The Canadian Mineralogist*, **37**, 1261−1268.

Back M.E., Grice J.D., Gault R.A., Cooper M.A., Walford P.C. and Mandarino J.A. (2017) Telluromandarinoite, a new tellurite mineral from the El Indio-Tambo mining property, Andes Mountains, Chile. *The Canadian Mineralogist*, **55**, 21−28.

Brugger J., Etschmann B.E., Grundler P.V., Liu W., Testemale D. and Pring A. (2012) XAS evidence for the stability of polytellurides in hydrothermal fluids up to 599 C, 800 bar. *American Mineralogist*, **97**, 1519−22.

Bruker (2001) *SADABS* and *XPREP*. Bruker AXS Inc., Madison, WI, USA.

Cametti G., Churakov S., and Armbruster T. (2017) Reinvestigation of the zemannite structure and its dehydration behavior: a single-crystal X-ray and atomistic simulation study. *European Journal of Mineralogy*, **29**, 53−61.

Christy A.G. (2015) Causes of anomalous mineralogical diversity in the Periodic Table, *Mineralogical Magazine*, **79**, 33−50.

Christy A.G. and Mills S.J. (2013) Effect of lone-pair stereoactivity on polyhedral volume and structural flexibility: application to $Te^{IV}O_6$ octahedra. *Acta Crystallographica*, **B69**, 446−56.

Christy A. G., Mills S. J. and Kampf A. R. (2016) A review of the structural architecture of tellurium oxycompounds. *Mineralogical Magazine*, **80**, 415−545.

Clarke R.M. (1997) Saddlebackite, $Pb_2Bi_2Te_2S_3$, a new mineral species from the Boddington gold deposit, Western Australia. *Australian Journal of Mineralogy*, **3**, 119−124.

Coats R.P. and Blissett A.H. (1971) Regional and economic geology of the Mount Painter province. Department of Mines, G*eological Survey of South Australia Bulletin*, **43**, 426 pp.

Cooper M.A, Hawthorne F.C., Abdu Y.A., Walford P.C. and Back M.E. (2019) Relative humidity as a driver of structural change in three new ferric-sulfate-tellurite hydrates: New minerals tamboite and metatamboite, and a lower-hydrate derivative, possibly involving direct uptake of atmospheric $\{H_2O\}_4$ clusters. *The Canadian Mineralogist*, **57**, 605−635.

Eder F., Marsollier A. and Weil M. (2023a) Structural studies on synthetic $A_{2−x}[M_2(TeO_3)_3]\cdot nH_2O$ phases (A = Na, K, Rb, Cs; M = Mn, Co, Ni, Cu, Zn) with zemannite-type structures. *Mineralogy and Petrology*, **117**, 145−163, https://doi.org/10.1007/s00710-023-00814-5

Eder F., Weil M. and Miletich R. (2023b) $K[(Cu^{II},Mn^{II},Mn^{III})_2(TeO_3)_3]\cdot 2H_2O$, the first zemannite-type structure based on a Jahn-Teller-distorted framework. *Mineralogy and Petrology*, **117**, 133−143, https://doi.org/10.1007/s00710-022-00808-9.

Effenberger H. S., Ende M. and Miletich R. (2023) New insights into the crystal chemistry of zemannite: Trigonal rather than hexagonal symmetry due to ordering within the host-guest structure. *Mineralogy and Petrolog*y, **117**, 117−131, https://doi.org/10.1007/s00710-023-00820-7.

Gagné O.C. and Hawthorne F.C. (2015) Comprehensive derivation of bond-valence parameters for ion pairs involving oxygen. *Acta Crystallographica*, **B71**, 562−578.

Grundler P.V Brugger J., Etschmann B.E., Helm L., Liu W., Spry P.G., Tian Y., Testemale D. and Pring A. (2013) Speciation of aqueous tellurium(IV) in hydrothermal solutions and vapors, and the role of oxidized tellurium species in Te transport and gold deposition. *Geochimica et Cosmochimica Acta*, **120**, 298−325.

Hamisi J., Etschmann B., Tomkins A., Pitcairn I., Wlodek A., Morrissey L., Micklethwaite S., Trcera N., Mills S. and Brugger J. (2023). Complex sulfur speciation in scapolite − implications for the role of scapolite as a redox and fluid chemistry buffer in crustal fluids. *Gondwana Research*, **121**, 418−435, https://doi.org/https://doi.org/10.1016/j.gr.2023.05.005

Higgin A.J. (1899) Notes on melonite (nickel-telluride) from Worturpa, South Australia. *Transactions of the Royal Society of South Australia*, **23**, 211−212.

Kabsch W. (2010) XDS. *Acta Crystallographica*, D66, 125−132.

Koyama E. and Nagashima K. (1981) Kinichilite, a new mineral from the Kawazu mine, Shimoda city, Japan. *Mineralogical Journal*, **10**, 333−337.

Krivovichev V.G., Krivovichev S.V. and Charykova M.V. (2020) Tellurium minerals: structural and chemical diversity and complexity. *Minerals*, **10**, 623.

Laugier J. and Bochu B. (2004) *Chekcell: Graphical Powder Indexing Cell and Space Group Assignment Software*. Available at http://www.ccp14.ac.uk/tutorial/lmgp/

Miletich R. (1995a) Crystal chemistry of the microporous tellurite minerals zemannite and kinichilite, $Mg_{0.5}[Me^{2+}Fe^{3+}(TeO_3)_3]\cdot 4.5H_2O$, $(Me^{2+}=Zn;$ Mn). *European Journal of Mineralogy*, **7**, 509−524.

Miletich R. (1995b) The synthetic microporous tellurites $Na_2[Me_2(TeO_3)_3]\cdot 3H_2O$ (Me = Zn, Co): crystal structure, de-and rehydration, and ion exchange properties. *Monatshefte für Chemie/Chemical Monthly*, **126**, 417−430.

Mills S.J. and Christy A.G. (2013) Revised values of the bond-valence parameters for Te^{IV}-O, Te^{VI}-O and Te^{IV}-Cl. *Acta Crystallographica*, **B69**, 145−149.

Missen O.P., Mills S.J., Spratt J., Birch W.D. and Brugger J. (2019a) Crystal chemistry of zemannite-type structures: I. A re-examination of zemannite from Moctezuma, Mexico. *European Journal of Mineralogy*, **31**, 519−527.

Missen O.P., Mills S.J., and Spratt J. (2019b) Crystal chemistry of zemannite-type structures: II. Synthetic sodium zemannite. *European Journal of Mineralogy*, **31**, 529–536.

Missen O.P., Back M.E., Mills S.J., Roberts A.C., LePage Y., Pinch W.W. and Mandarino J.A. (2021) Crystal chemistry of zemannite-type structures: III. Keystoneite, the Ni^{2+}-analogue of zemannite, and ferrotellurite discredited. *The Canadian Mineralogist*, **59**, 1–10.

Missen O.P., Mills S.J., Brugger J., Birch W.D. and Elliott P. (2023) Wortupaite, IMA 2022–107. CNMNC Newsletter 71. *Mineralogical Magazine*, **87**, 332–335, https://doi.org/10.1180/mgm.2023.11

Momma K and Izumi F (2011) VESTA 3 for three-dimensional visualization of crystal, volumetric and morphology data. Journal of Applied Crystallography, **44**, 1272–1276.

Pekov I.V., Siidra O.I., Vlasov E.A., Yapaskurt V.O., Polekhovsky Y.S. and Apletalin A.V., (2018) Ilirneyite, $Mg_{0.5}[ZnMn^{3+}(TeO_3)_3] \cdot 4.5H_2O$, a New Mineral from Chukotka, Russia. *The Canadian Mineralogist*, **56**, 1–9.

Rempel K. and Stanley C.J. (2016) Kalgoorlieite, IMA 2015–119. CNMNC Newsletter No. 30, April 2016, page 412; *Mineralogical Magazine*, **80**, 407–413.

Rice C.M., Welch M.D., Still J.W., Criddle A.J. and Stanley C.J (2016) Honeaite, a new gold-thallium-telluride from the Eastern Goldfields, Yilgarn Craton, Western Australia. *European Journal of Mineralogy*, **28**, 979–990.

Sheldrick G.M. (2015a) SHELXT – Integrated spacegroup and crystal-structure determination. *Acta Crystallographica*, **A71**, 3–8.

Sheldrick G.M. (2015b) Crystal structure refinement with SHELXL. *Acta Crystallographica*, **C71**, 3–8.

Welch M.D., Still J.W., Rice C.M., Stanley C.J. and Hibbs D. (2017) A new telluride topology: the crystal structure of honeaite Au_3TlTe_2. *Mineralogical Magazine*, **81**, 611–618.

Wildner M. (1993) Zemannite-type selenites: crystal structures of $K_2[Co_2(SeO_3)_3] \cdot 2H_2O$ and $K_2[Ni_2(SeO_3)_3] \cdot 2H_2O$. *Mineralogy and Petrology*, **48**, 215–225.